FULL RESEARCH ARTICLE

Powder bed fusion of solid and permeable Crofer 22 APU parts for applications in chemical process engineering

Masoud Mahmoudizadeh[1] · Christoph Klahn[2] · Roland Dittmeyer[1]

Abstract

Additive manufacturing of metals has attracted significant attention across various industries. However, its adoption in certain chemical and energy sectors remains constrained by the absence of optimized alloys tailored for high temperatures and corrosive environments. This study explores the laser-based powder bed fusion processing of Crofer 22 APU, a high-temperature, corrosion-resistant alloy ideal for applications such as methane steam reforming reactors, high-temperature fuel cells, and palladium membrane supports. Systematic optimization of laser parameters including laser power, hatch distance, point distance, and building angles was conducted for both dense and porous objects. Dense parts achieved a relative density of 0.9999 and surface roughness of Sa= 41.27±1.48 on a 45° overhang. Porous samples showed a porosity range of 28.655.5% and surface roughness Sa 22.2 µm to 45.9 µm as hatch distance increased from 0.12 mm to 0.16 mm. Additionally, an 8YSZ coating applied via screen printing demonstrated the impact of hatch distance and laser power on surface quality. The combination of additive manufacturing of Crofer 22 APU and screen printing of 8YSZ simplifies the preparation of metallic supports for Pd-based membranes, reducing fabrication time and cost by shortening the number of preparation steps. This technique offers a promising approach for scaling up membranes and membrane reactors.

Keywords Laser-based powder bed fusion of metals (PBF-LB/M) · Crofer 22 APU · Permeable material · Membrane reactor · Coating

1 Introduction

1.1 Hydrogen production

Hydrogen is a key energy vector for industries such as steel production, glass manufacturing, copper processing, and hardening industries. However, delivering hydrogen to users from a centralized gas plant results in additional CO_2 emissions during transportation and raises safety concerns [1]. Currently, around 96% of hydrogen is produced from fossil fuels like natural gas (NG), coal, and oil. Hydrogen production from NG and steam is the globally dominant process.

Natural gas primarily consists of a large amount of CH_4, along with smaller quantities of C2–C4 fractions, CO_2, and H_2S. Methane steam reforming (MSR) is an energy-intensive reaction that increases gas volume. The reaction is thermodynamically favored at high temperatures and low pressure, operating at temperatures ranging from 700 to 1000 °C and pressures of 3 to 25 bar [2]. The MSR process provides the highest ratio of H_2/CO and yields the maximum amount of H_2. This is primarily because most of the generated CO is further converted into CO_2 and H_2 through the water-gas shift reaction.

The water gas shift reaction is exothermic and favored at lower temperatures, while the pressure does not affect its thermodynamics. More information about the MSR can be found in the following references [3–6]. Configuration of such systems for decentralized hydrogen supply in some cases demands a compact production and gas separation unit. Ultra-compact membrane reactors (MR) are promising options for hydrogen production from natural gas or biogas, where a catalytic reactor is coupled to a self-supported/supported palladium-based membrane [7–9].

✉ Masoud Mahmoudizadeh
  masoud.mahmoudizadeh@kit.edu

1 Karlsruhe Institute of Technology (KIT), Institute for Micro Process Engineering (IMVT), 76344 Eggenstein-Leopoldshafen, Germany

2 Karlsruhe Institute of Technology (KIT), Institute of Mechanical Process Engineering and Mechanics (MVM), 76131 Karlsruhe, Germany

Since Pd or Pd-alloys are highly expensive, they are preferably coated as thin layers on either metallic porous or ceramic supports. Compared to ceramic supports, metal supports offer the advantage of better heat conduction, mechanical stability, and an easier integration of the parts using methods such as welding [10, 11].

1.2 Metallic porous substrates

The exploration of materials for metallic supports in Pd composite membranes has been extensively examined in the existing literature. Various manufacturers globally have been taken into account, including Mott Metallurgical Corp. (USA), Pall Corp. (USA), and GKN Sinter Metal (UK) [12]. Table 1 displays a compilation of metallic supports available commercially from various companies. Nevertheless, the criteria to be considered when choosing a metallic support encompass factors such as thermal expansion coefficients (e.g., ferritic stainless steels) compatibility with other membrane components like Pd, the final surface quality for Pd coating, mechanical and chemical stability for applications such as steam reforming for hydrogen production, and thermal stability for long-term operation at moderate and elevated temperatures. In this study, Crofer 22 APU demonstrates an advantageous capability in meeting these requirements.

1.3 Connecting metallic porous substrates to dense frames

The metallic porous substrates need to be connected to a frame for assembly and sealing purposes. Typically, these components are joined together through welding. For example, the use of laser welding to join the porous sintered metal of Crofer 22 APU to a dense frame of the same material is shown in Fig. 1. By welding a gas-permeable sinter-metal made of Crofer 22 APU to a dense frame of the same material, a hybrid form of dense/porous metallic membrane support is created. This structure can then be coated with an intermediate layer, followed by a thin layer of Pd coating. Additional details can be found in references [1, 18].
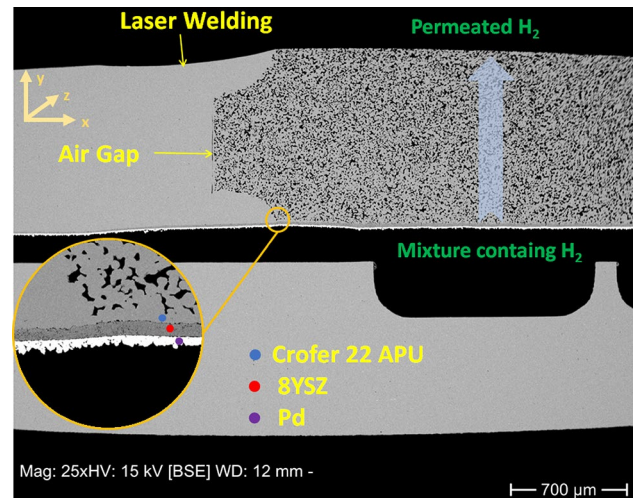
Fig. 1 Cross-sectional view of a composite Pd membrane consisting of porous sinter metal of Crofer 22 APU, 8YSZ diffusion barrier layer, and Pd layer (selective towards hydrogen) for hydrogen separation from a gas mixture. More details regarding the Pd coating can be found in [18]. In the described system, H_2 is separated from the feed side to the permeate side in the y-direction. The gas flow occurs in the z-direction

Although laser welding is an efficient technique, its weld seam (see Fig. 1) causes problems in subsequent coatings. Xie and Dittmeyer [19] have described these challenges and proposed a possible solution using additively manufactured plates. However, the proof-of-concept part was still made of stainless steel 316 L, which is not the optimal choice concerning compatibility with Pd and working at elevated temperatures e.g., above 500 °C. Our recent studies on additive manufacturing (AM) motivated us use this technique for a practical MR system by developing metal additive manufacturing process parameters for Crofer 22 APU.

1.4 Additive manufacturing

The additive manufacturing technology of laser-based powder bed fusion of metals (PBF-LB/M) is a mature production process for creating complex monolithic parts and

Table 1 The thermal expansion coefficient of the principal elements in a metallic composite, Pd-based membrane designed for H_2 separation

Material	Property	CET ($1 \times 10^{-6} K^{-1}$)	Ref
Pd	Selective towards H_2	12.26 at 525 °C	[13]
8-YSZ (TZ-8Y Tosoh)	Reducing pores for Pd coating, metal inter-diffusion mitigation	10.5–10.7	
Crofer 22 APU	Membrane support, MR body	10.3–11.2 at 500 °C	[14]
Hastelloy X	Metallic filter	14.5–15.5 at 500 °C	[15]
Inconel 600	Metallic filter	14–15.5 at 500 °C	[16]
AISI 316 L	Metallic filter	18 at 500 °C	[17]
AISI 304 SS	Metallic filter	18 at 500 °C	[17]

individualized designs. The field of process engineering already benefits from well-known properties such as the porosity of the structure and structured supports, which improve heat and mass transfer by increasing the exposed surface area. This is achieved through optimized and compact chemical devices [20–22].

A literature review found no suitable AM high-temperature alloys for Pd membrane supports. The classification of high-temperature alloys is based on a functionality, working in the range of 30% to 70% of the desired alloy's melting temperature [23]. Temperature is one of the important parameters to select the material for a system, especially a multi-component system like a MR. Rizzi et al [23] present a comprehensive review of alloys for high-temperature applications in chemical industries. Nevertheless, none of the commercially available AM materials for high temperature are deemed suitable.

AM can be used to fabricate metallic supports for a Pd-based composite membrane. As shown in Fig. 1 and compared with Fig. 2, AM can replace the conventional technique of metallic support preparation by welding. In the conventional method, the frame and porous parts are cut, machined (in the case of forming micro-channels on the plates), post-processed, and coated in sequence. AM can reduce these steps as well as that AM eliminates welding effects at the interface of dense and porous parts, providing a smoother surface for coating thin layers.

Moreover, the role of AM can be further highlighted when printing several functional plates for an MR together in one job.

For instance, as shown in Fig. 3, by additive manufacturing the plate (No. 11 instead of No. 4–9), the final cell (including whole plates) undergoes not only less thermal stress when laser welding but also might be produced in thinner thickness (plate No. 11 saves up to 2 mm in thickness). The idea of such a planner structure allows to scale-up the system through the number of stacks, while the ratio of the surface area of the membrane to the volume of the system remains high. Regarding the application of such a system, it is important to note that H_2 is often used as a reducing agent in certain industries. This is typically achieved by using a diluted mixture of H_2 with an inert gas like N_2 in processes such as hardening, steel production, and glass manufacturing. One example involves using a decentralized H_2 supply system, similar to the one depicted in Fig. 3, to provide 50 N m^3h^{-1} of a minimum 3% H_2 in H_2 mixture for hardening applications. For such a compact system, AM can be utilized to create at least composite multi-functional plates as previously discussed. The potential for using AM to manufacture the entire MR will be explored in future
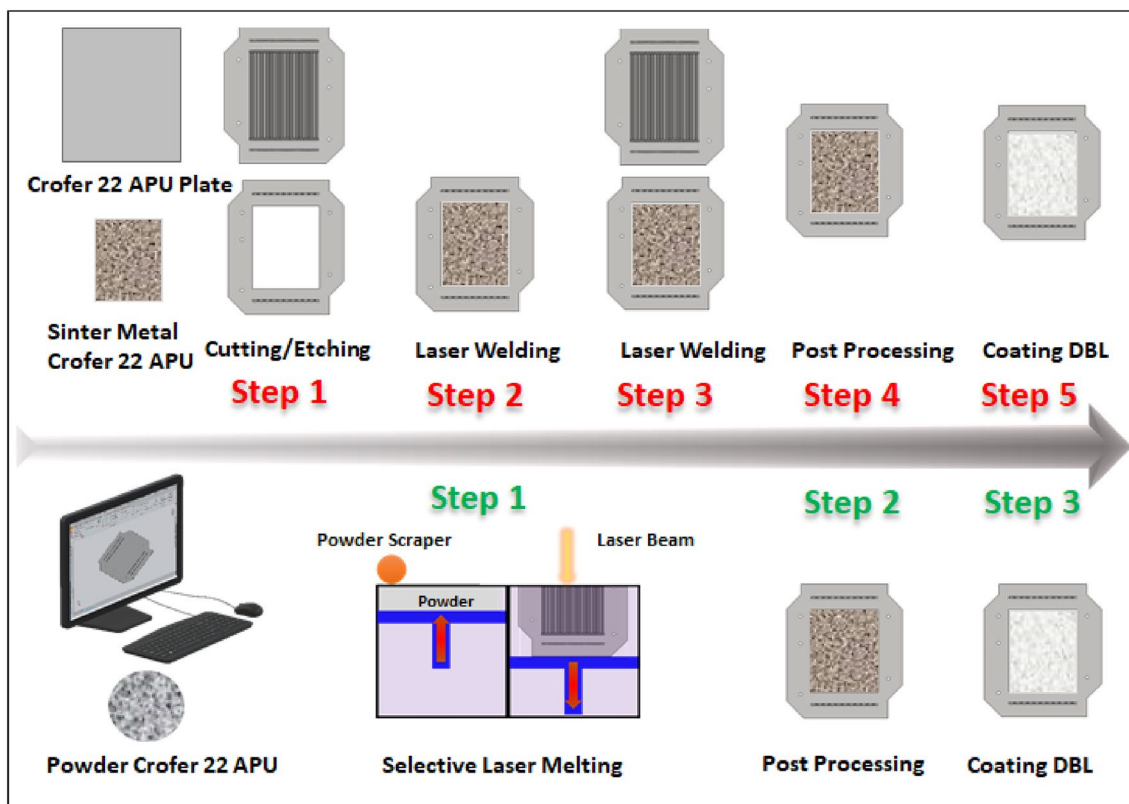

Fig. 2 Comparison of preparation of planar metal-based membrane support through PBF-LB/M and tape-casting plus welding techniques

Fig. 3 One-go printing of integrated plates of an MR with the PBF-LB/M technique (No. 4–9); printing the composite porous-dense plate (No. 11), thickness of 3 mm

No.	Name/thickness (mm)
1	Cover plate/2
2	Pre-reformer plate/1
3	Reformer plate/2
4	Membrane plate/1
5	Permeate plate/1
6	Interplate1/1
7	Interplate 2/1
8	Combustor plate/1
9	Air distributor plate/1
10	Cover plate/2
11	AM of plates No. 4-9/3
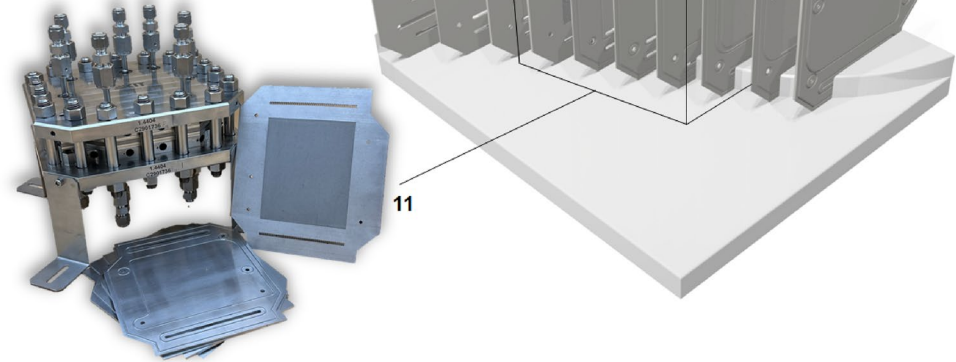
studies and is beyond the scope of this research. Moreover, the process prospect and system performance will be separately discussed in the future. This study focuses on a novel approach to chemical reactor and metallic membrane support design by optimizing the parameters for PBF-LB/M in the manufacturing of parts for high-temperature applications, particularly in the hydrogen production and separation industry. By refining these parameters, the research aims to enhance process efficiency through more compact designs and produce more stable parts for long-term operation using AM of Crofer 22 APU.

2 Additive manufactured permeable structures

Stoffregen et al. [24] distinguish two approaches to producing permeable AM material: The creation of an undefined pore structure by choosing process parameters with lower energy input or the creation of a geometrically defined structure. Gu and Shen [25] produced permeable 316 L (1.4404) stainless steel by adjusting the laser process parameters. Yadroitsev et al [26] demonstrated with stainless steels 316 L and 904 L (1.4539) that a geometrically defined approach offers more control over the size, shape, and distribution of pores. Thin walls with intermediate gaps are formed by placing the individual melt tracks on top of each other. The resulting porosity consists mostly of through pores that contribute to the permeability of the material while undesired blind or closed pores are avoided. Blind and closed pores reduce the strength and fatigue life of a part without contributing to the permeability. We favor the

term *permeable material* for such materials to distinguish the functional structure from an undesired random porosity.

The permeability of geometrically defined structures is not necessarily isotropic. The permeable material consists of an arrangement of straight walls made from stacked melt tracks with open gaps between them. The arrangement of melt tracks in the scan strategy defines the orientation of the gaps and therefore the main direction of flow. Klahn [27, 28] equipped parts with large permeable areas with a flow direction aligned with the build direction. He demonstrated the viability of such permeable structures made from tooling steel Maraging 300 (1.2709) in the mechanically challenging application of pneumatic ejectors for injection molding tools. Xie and Dittmeyer [19] developed a scan strategy for large, planar surfaces with a flow direction perpendicular to the build direction. Later, their approach was extended to tubular parts with a flow direction radial to the build direction [29].

The most common approach for permeable/dense composite parts is to separate the part into individual 3D models for each type of material. Klahn [27] and Xie et al. [29] demonstrated the feasibility and design opportunities of integrating multiple types of permeable materials into a single part. A suitable parameter set is assigned to each 3D model to achieve different gap sizes, orientations or patterns. Li et al. [30] proposed a similar approach for undefined pore structures to create a gradient porous structure with varying pore sizes.

The stacked melt tracks provide less volume for heat conduction and as heat sink. Consequently, the melt temperature rises and melt volume increases. The increased melt volume leads to elevated melt tracks. Yasa et al. [31] associates

elevated edges to melt flow and process parameters. Manufacturing permeable material requires an adaptation of the process parameters of the laser-based powder bed fusion process. Documented process parameters for permeable materials show a decrease of laser power P_L and an increase in scan speed v_S to reduce the energy density of the laser-based powder bed fusion process [19, 25, 27].

3 Additive manufacturing of Crofer 22 APU for dense/permeable composite parts

The membrane reactor requires a high-temperature steel with a thermal expansion coefficient similar to that of the one of the ceramic coating. The stainless steel Crofer 22 APU exhibits these properties because it was developed for Solid Oxide Fuel Cells (SOFC) and Solid Oxide Electrolytic Cells (SOEC) stacks [14]. These applications demand high temperature and corrosion resistance, as well as a thermal expansion coefficient that matches the ceramics typically used in fuel cells.

Crofer 22 APU (1.4760, X1CrTiLa22, ASTM A240) is a ferritic stainless steel. Its composition is listed in Table 2. The alloy manufacturer VDM Metals states that the material may contain additional elements for technical reasons [14]. The analysis of the virgin powder used in this study by the powder supplier Rosswag indicates that the material meets the specifications of the alloy manufacturer, except for a lower concentration of Lanthanum.

Despite the impact on alloy properties due to the reduction in lanthanum (La) content during gas atomization, Crofer 22 APU remains suitable for applications at temperatures below 900 °C. At such elevated temperatures, the volatility of chromium oxide becomes a concern, and the addition of a minimal amount of La effectively addresses this issue. However, for processes like MSR that operate within a range from moderate to relatively high temperatures, Crofer 22 APU remains a favorable choice. Its ferritic nature and compatibility with Pd in an MSR system make it a robust and viable option.

The Crofer 22 APU bulk material was gas atomized into a fine powder consisting of spherical particles. Figure 4 shows the particle size distribution of the virgin powder.

A parameter study on a DMG Realizer SLM-125 laser-based powder bed fusion machine identified the parameters listed in Table 4 for the production of dense and permeable structures. The scan strategy for dense parts is a typical island strategy with 5 mm squares and a variation of the island positions and orientations between layers. The permeable parts are manufactured by increasing the hatch distance h_s to create a gap between neighboring melt tracks. The melt tracks are unidirectional and parallel to the flow direction of the MR. This pattern remains consistent across all layers of the permeable section of the membrane part.

3.1 Characterization of dense parts

3.1.1 Relative density

To find the optimal parameter for printing a gas-tight part (dense part), a set of hatching parameters was considered (illustrated in Table S1). The printed objects were in form of cubes with a length of 10 mm. After the build job, the samples were separated from the build plate and rinsed with isopropanol to remove loose powder particles. They were subjected to polishing treatment before imaging, as
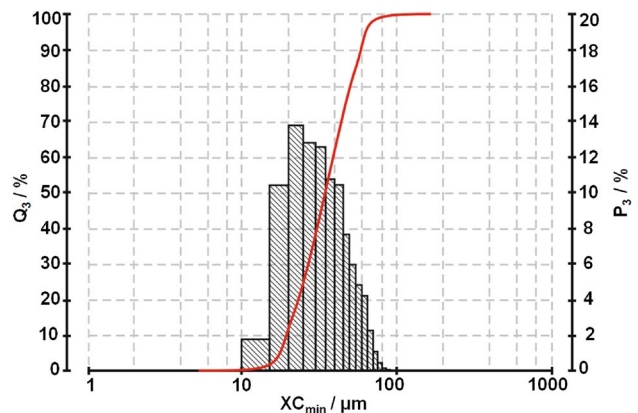

Fig. 4 Particle size distribution of the Crofer 22 APU powder

Table 2 Chemical composition of Crofer 22 APU in [%], min. and max. by specification [14] and analysis of the virgin powder

	C	Cr	Fe	S	Mn	Si	Ti	Cu
Min. [14]		20.0	Bal		0.30		0.03	
Max. [14]	0.03	24.0		0.020	0.80	0.50	0.20	0.50
Analysis	<0.01	22.21	Bal	<0.003	0.38	0.02	0.06	0.01
	P	Al	La	Mo	Ni	V	W	Co
Min. [14]			0.04	n.s	n.s	n.s	n.s	n.s
Max. [14]	0.050	0.50	0.2	n.s	n.s	n.s	n.s	n.s
Analysis	0.006	0.013	<0.005	0.02	0.02	0.01	<0.01	0.01

follows. To achieve a mirror-polished finish for the printed samples, essential for analyzing porosity and defects, the ATM SAPHIR 550 polishing machine was utilized, featuring a holder and a cooling water system. The stepwise polishing procedure involved the successive use of finer polishing papers: starting with number 320, followed by 400, 600, and 1200, each for 2 min at a rotation speed of 300 rpm. Subsequently, an additional 2 min of polishing with paper number 2500 at a reduced speed of 150 rpm was carried out. In the final stages, the samples were polished with Dia-COMPLETE poly pastes, first with 3 µm and then with 1 µm pastes, each for an additional 2 min at 150 rpm. This consistent treatment approach was also applied to polish the cross-sections of the samples, preparing them for subsequent SEM analysis. All samples underwent measurement using a single SENSOFAR SNEOX optical profilometer, employing various techniques for quantitative characterization. The measurement techniques of Imaging Confocal Microscopy was used for whole samples. Consistent conditions were maintained with 10x magnification at identical Region of Interest (ROI) locations (at least 3 spots on each sample) for the measuring technique, covering an area of 1.75×1.32 mm^2. Data processing was carried out using SensoSCAN 6.4 software. Initially, non-measured points were computed as a performance indicator and then reconstructed by interpolation using the "smooth shape calculated from the neighbors" algorithm. A least-squares plane fitting, implemented as the F-operator, removed the global form of the surfaces analyzed in the study. No L-filter (high-pass filter) was applied, preserving all topographic features of the additive manufacturing process. A set of topographical parameters from ISO 25178, related to height (S_q, S_{sk}, S_{ku}, S_a), spatial (S_{al}), and hybrid (S_{dr}) were calculated on the primary surface.

A MATLAB code was used to determine the potential pore quantity and diameter on the surface from the images. Briefly, in the quantitative analysis of 3D-printed samples across diverse research domains using MATLAB, the initial step involved the conversion of images into a binary format. This conversion required assigning gray values to pixels within the range of 0 to 255. Consequently, the binary images exhibited a clear black-and-white contrast, effectively revealing the internal structure. In this binary representation, pixels with a value of 0 represented black and corresponded to pores, while pixels with a value of 255 were depicted as white, signifying the non-porous area. The binarization process was executed using MATLAB's native "Color Thresholder" application. After having the images, binary images are generated. Further analysis includes calculating parameters such as image porosity, and pores size distribution were carried out. The 'size' function in MATLAB is utilized to identify and extract pixels in the binary image. Employing the built-in 'bwarea' function, the total number of image points, representing the sum of black and white pixels, can be obtained. The porosity is calculated based on dividing the black pixels to the whole pixels. Additionally, to analyze the distribution of pore radius, the 'bwlabel' function in MATLAB is utilized (see Figure S2).

The results showed that the sample with the hatching parameter H08 (Laser current L_C: 2000 mA, point distance P_D: 35 µm, scan speed v_s: 1750 mm s^{-1}) represents the minimum defects and a relative density of 0.9999.

3.1.2 Surface roughness

The surface quality for different orientations and the need for support structures are also affected by process parameters. In this regard, the surface roughness Sa depending on the down-facing angles of the objects is characterized on samples depicted in Figure 5 [32]. The design was chosen because it allows the evaluation of up- and down-facing surfaces in two opposing orientations. The size of samples allows for measuring at least 5 points on each surface according to the reference [32]. This set of samples allows the characterization of surfaces with angles $\alpha = 25°, 35°, 45°, 90°, 135°, 145°$ and $155°$. The roughness was measured based on areal average roughness (S_a). By comparing Table 3, Table S1, and also Figure S5, it is seen that samples with contour parameters C02 and C03 show

Table 3 Arithmetical mean height of the surface *Sa* of additive manufactured Crofer 22 APU with a surface angle *α* to the build plate

Sample	Down-facing surfaces				Up-facing surfaces		
	25°	35°	45°	90°	135°	145°	155°
C01	83.86±8.27	49.89±2.22	32.99±2.05	33.76±2.00	37.46±3.51	44.03±2.85	51.68±7.78
C02	61.65±3.80	47.05±2.33	41.27±1.48	26.15±2.57	31.34±2.77	28.98±2.92	34.24±1.85
C03	62.57±6.80	45.74±3.85	41.55±2.06	26.68±1.29	28.43±3.87	30.49±2.94	40.09±1.51
C04	50.82±4.99	49.95±1.84	44.89±4.32	27.11±0.61	43.64±2.56	39.74±4.09	44.96±5.30
C05	106.47±9.18	94.05±5.10	60.56±4.59	14.08±2.22	30.03±5.36	38.35±2.60	44.87±6.83
C06	89.18±4.08	109.32±11.31	78.60±13.17	18.31±0.69	30.62±2.97	41.98±9.33	49.81±5.52
C07.90°	114.06±12.84	104.76±15.80	55.58±4.67	13.31±0.56	25.09±5.11	37.90±7.99	43.76±7.50
C08.90°	102.10±14.20	88.49±7.48	67.76±10.62	12.42±0.17	33.78±5.56	54.07±8.01	53.23±11.48
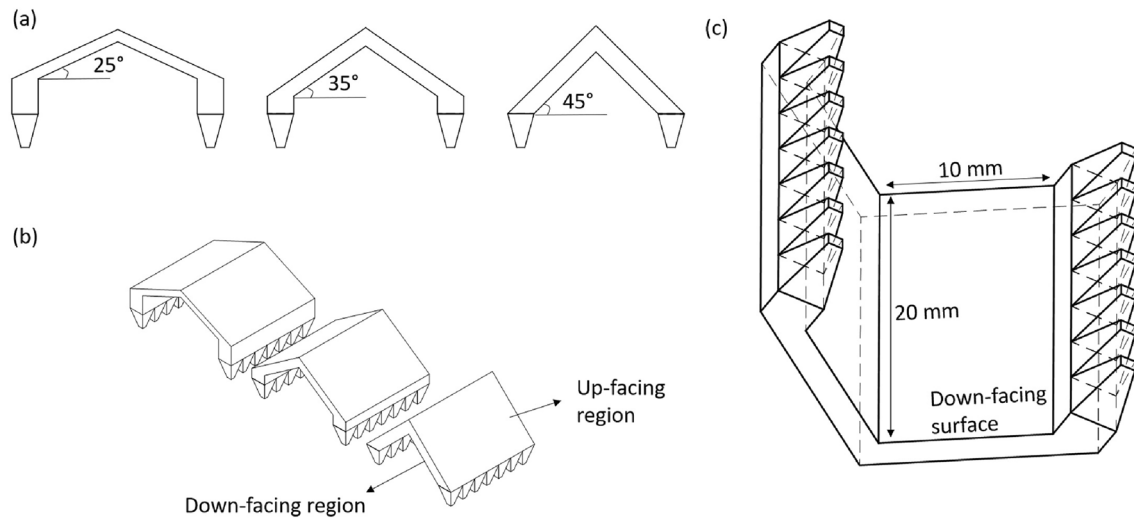
Fig. 5 Sample for the evaluation of surface roughness of AM Crofer 22 APU, **a** Front view of manufactured test pieces showing all three printed angles 25°, 35° and 45°, **b** isometric view of printed test pieces and **c** view of down-facing surface of all test pieces [32]

lower surface roughness (L_c: 1400 mA and P_D: 30 µm and 40 µm, respectively), compared to the those of other samples, except the angle 25°. Compared to up-facing surfaces 135°-155°, the down-facing surfaces are susceptible to dross formation as the penetration of melt pool into the powder bed increases causing higher surface roughness. Such a high roughness could be critical when coating onto a printed reactor wall, as it may hinder the formation of an even and homogeneous layer. However, defining one set of parameters that meets the surface quality for all regions of a complex geometry remains a challenge. Ferchow et al. [33] extended the feasibility of overhanging geometries by assigning different parameter sets to different regions. They showed that it is possible to reduce the post-processing efforts. Accordingly, depending on the target geometry for a reactor body, sets of parameters can be selected from Table 3.

As a conclusion, Table 4 lists the optimal parameters to print dense parts from Crofer 22 APU. The parameters on Realizer machines are converted in the usual PBF-LB/M parameters. With these parameters, a relative density of 0.9999 and a surface roughness Sa = 41.27±1.48 at $\alpha = 45°$ and Sa = 26.15±2.57 at $\alpha = 90°$ were achieved. In the following section, the permeable part is discussed.

3.2 Characterization of permeable parts

After achieving a rather defect-free wall, the next step was to study of the permeable parts. Eight cubes were manufactured with the parameters S1-S8 listed in Table 5. They were polished and mounted in epoxy, as shown in Fig. 6. This Figure demonstrates that with an increase in the hatch distance from 0.12 mm to 0.16 mm, the porosity based on the surface

Table 4 Process parameters for dense part printing with Crofer 22 APU powder

|	Hatch (H08)	Contour (C02)
Laser power P_L (W)	180	180
Laser current L_c (mA)	1800	1800
Scan speed v_s (mm s^{-1})	1750	750
Hatch distance h_s (µm)	80	–
Layer thickness s (µm)	50	50

images, increases by approximately 19% and 14% for a laser current 1000 mA and 1200 mA, respectively.

In another print job, the samples were printed in a plate shape with dense frames for a water permeability test. The test was carried out on the as-received samples using a flow cell system to estimate the superficial velocity versus pressure drop. The permeability assessment involved utilizing a flow cell system to measure the pressure loss at various flow rates of water passing through the test sample. The initial step included polishing the dense part for better sealing. Subsequently, sealing the dense part of the tested sample was accomplished using rubber sealings. Pressure measurements were conducted using a Baumer PBSN pressure sensor, which had a range from 0bar to 2.5bar absolute and a standard error of measurement of ± 0.03% FSP.

The Verdergear VG 1000 basic gear pump controlled the water flow rate, which was adjusted within the range of 30% to 80% of the maximum rating of 4000 rpm, with 10% intervals. The precise determination of each setting was achieved by measuring the amount of water permeating over 2 min. Before each permeation test, the flow cell system ran for 30 min to ensure stable conditions, including complete wetting of the

Fig. 6 Top view and cross-sectional view of printed samples with different hatch distances and laser power (hatch distance 0.12–0.16 mm and laser current 1000–1200 mA)
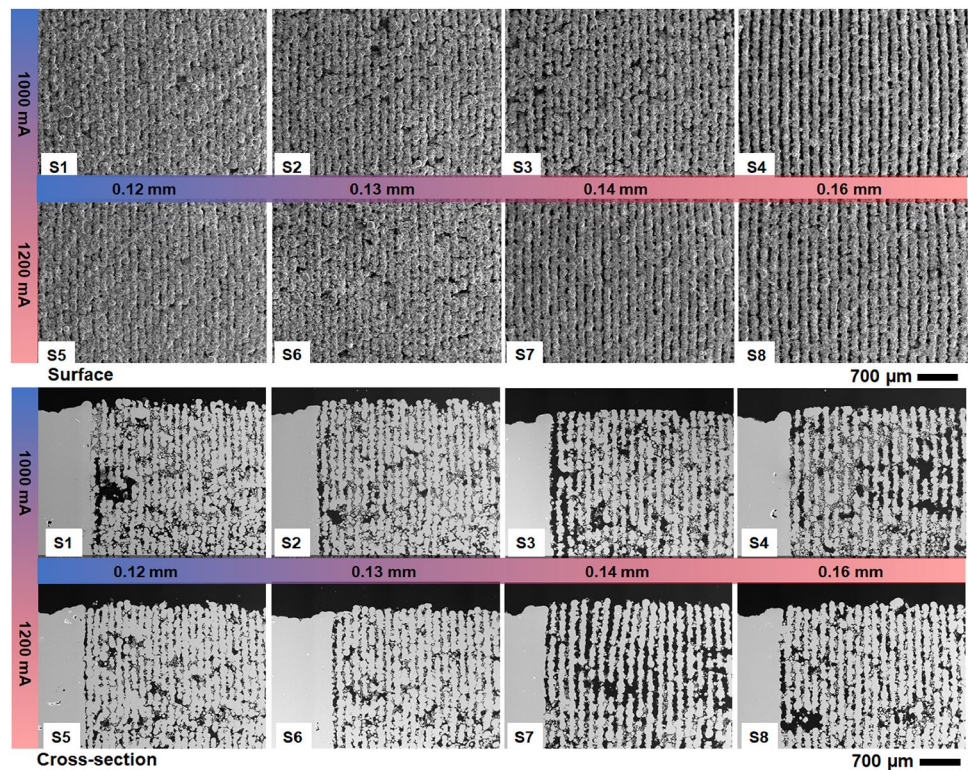
sample, a constant flow rate, and pressure loss. Throughout the measurement procedure, the system was allowed to equilibrate for at least 5 min after setting a higher flux before measuring the corresponding pressure loss. The superficial velocity was then calculated based on the amount of water permeating within 120 s using the formula specified in Equation 1.

$$v = \frac{m_{H_2O}}{\Delta t} \rho_{H_2O}^{-1} A_{porous}^{-1} \tag{1}$$

where $\rho_{H_2O} = 998$ kg m^{-3} and $A_{porous} = 2.2$ cm^2 were used for calculations. The flow behavior in the porous media is addressed in different ways [34–37]. Darcy's Law predicts the flow behavior in porous media , stating that the pressure gradient is linearly proportional to the fluid velocity. However, this linear dependency is only valid for low-pressure gradients or small flow velocities [38]. As the flow reaches a turbulent regime, a non-linear dependency of pressure gradient versus flow velocity is expected. Brinkman's equation describes the macroscopic fluid flow for laminar and turbulent regimes as follows:

$$\frac{\Delta p}{L} = \mu \frac{v}{K_D} + \rho \frac{v^2}{K_F} \tag{2}$$

with the speed v (m s^{-1}), pressure drop Δp (Pa) through the porous medium, the permeable part thickness L (m), fluid density ρ (kg m^{-3}) based on the inlet pressure, Darcy's K_D (m^2), and Forchheimer's terms K_F (m). To estimate the

porosity of the additively manufactured samples, porous parts with parameters S1–S8 were printed in disk shape with a diameter of 22 mm and a thickness of 1.1 mm. Equation 3 was used to estimate the corresponding porosity ϕ for each sample (see Table 3).

$$\phi = 1 - \frac{\frac{m_{exp}}{V_{exp}}}{\rho_{Crofer}} \tag{3}$$

where m_{exp} denotes the weight of samples measured by a balance (accuracy 0.1 mg) and V_{exp} is the volume of the printed disks. The density is $\rho_{Crofer} = 7.7$ g cm^{-1} according to the material certificate [14].

Figure 7 shows the results of the water permeability for samples S1-S8. It is observed that the permeability K_D increases from 2.77×10^{-12} to 1.98×10^{-9} m^2 for S1 (hatch distance 0.12 mm) compared to S4 (hatch distance 0.16 mm). The permeability also changes from 1.55×10^{-12} to 1.57×10^{-11} m^2 for S5-S8. Comparing S5 to S1, it is found that a laser current increase from 1000 mA to 1200 mA lowers K_D by approximately 44%.

These results confirm the feasibility and permeability for all parameters. The final choice of a parameter set depends on the ability to screen print a homogeneous layer of 8YSZ onto the permeable surface.
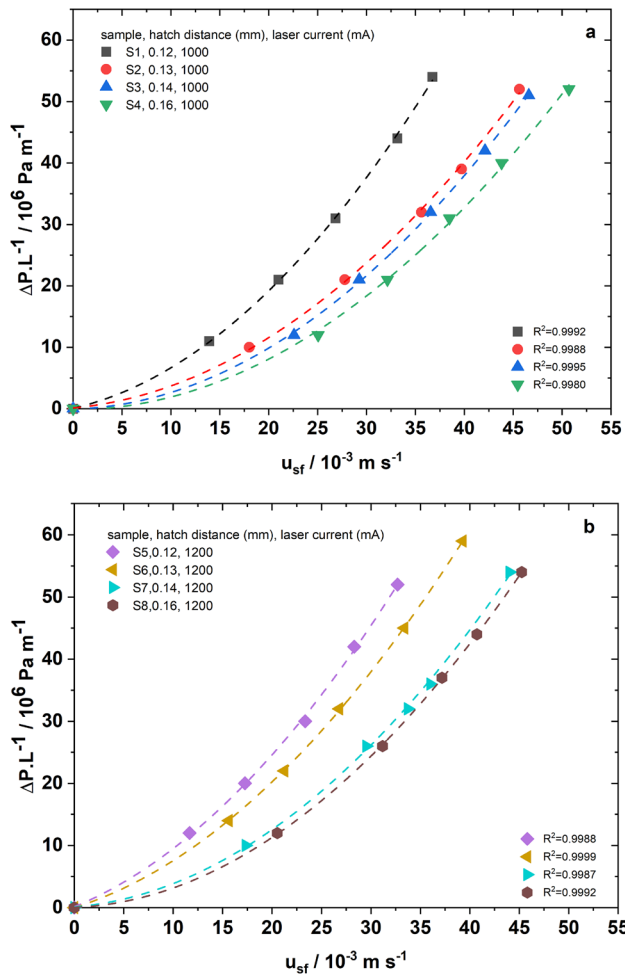
Fig. 7 Water permeability of additively manufactured samples (the y-axis represents the pressure gradient normalized by sample thickness, while the x-axis represents the velocity), effect of hatch distance ranging from 0.12 mm to 0.16 mm, **a** Laser current 1000 mA, **b** 1200 mA

4 Surface preparation for coating of active thin layers

Typically, preliminary treatments and modifications to a metallic support are carried out to enhance the overall quality of the membrane. Beyond standard initial cleaning procedures, the emphasis in most of these modifications lies in improving layer adhesion, reducing average pore sizes, and smoothing the support surface to achieve thin and defect-free Pd layers. These treatments can be categorized into three main types: (i) chemical treatment, such as using corrosive solutions, (ii) physical treatment, such as polishing; and (iii) incorporation of an intermediate layer. The following sections will discuss two specific techniques: heat treatment and ceramic layer coating (as an intermediate layer).

4.1 Microstructure of Crofer 22 APU before and after heat treatment

Annealing the metal substrates leads to the formation of a thin oxide layer that acts as a protective coating in the reactor. This oxide layer also enhances coating stability by providing a stable anchor for the coated layer. One sample (sample S5 which showed the lowest porosity among the samples) was heated up to 800 °C for 2 h. The EDS analysis was conducted on the surface of the porous part. Figure S1 shows sample S5 before (denoted as the fresh sample, after printing) and after annealing treatment. As it is seen, a layer of around 500 nm to 1000 nm on the outer surface is formed. Comparing the growth of the oxide layer, which reaches a maximum of approximately 1 mm, with the surface roughness reported for S5 (see Table 5), it appears that heat treatment has minimal impact on the surface roughness. Instead, it seems that the primary role of the formed layer is to act as a protective layer for the Pd layer. The formed layer shows a triangle structure for the grains near the surface.

In the literature, there are several examples of ferritic stainless steels forming two-layer oxide scales, with particular attention given to SS 430 [39–41]. Alloys of the

Table 5 calculated surface properties of the porous parts (hatch distance 0.12–0.16 mm and laser current 1000-1200 mA)

Sample	Hatch Distance (mm)	Laser current (mA)	Porosity ϵ (%)	Surface roughness Sa (μm)	K_D (m^2)	K_F (m)
S1	0.12	1000	33.87	23.70	2.77×10^{-12}	3.37×10^{-8}
S2	0.13	1000	35.91	26.04	7.02×10^{-12}	4.66×10^{-8}
S3	0.14	1000	41.40	31.06	2.25×10^{-11}	4.42×10^{-8}
S4	0.16	1000	55.47	44.96	1.98×10^{-9}	4.87×10^{-8}
S5	0.12	1200	28.62	23.30	1.55×10^{-12}	3.48×10^{-8}
S6	0.13	1200	31.63	22.17	1.99×10^{-12}	3.93×10^{-8}
S7	0.14	1200	34.44	25.50	7.77×10^{-12}	4.06×10^{-8}
S8	0.16	1200	44.41	40.91	1.57×10^{-11}	4.01×10^{-8}

Fe-Cr-Mn type exhibit a rapid formation of an initial Cr_2O_3 layer during oxidation. Saeki conducted a comprehensive study utilizing a combination of X-ray photoelectron spectrometry and XRD to characterize the oxides formed on SS 430 in an O_2/N_2 environment at 1000 °C for up to 20 min [39]. The investigation disclosed that within the first 15 s to 30s of oxidation, a single-phase oxide layer with a corundum structure is evident. Initially resembling Fe_2O_3 in chemical composition, this layer rapidly transitions to Cr_2O_3. After 30 s of oxidation, an $MnCr_2O_4$ spinel phase emerges, coinciding with a shift in the oxidation state of Mn from +3 (Mn_2O_3) to +2 ($MnCr_2O_4$). The study showed that the induction period for spinel formation corresponds to the time taken for Mn_2O_3 to reach its maximum solubility in Cr_2O_3 (12–17 wt.%). Once this threshold is exceeded, the $MnCr_2O_4$ spinel nucleates on the surface and grows through a reaction involving Mn_2O_3 and Cr_2O_3 [39, 40]. If this mechanism is applicable to the formation of the two-phase scale in the Crofer 22 APU samples under investigation, it suggests that the scale microstructure could be governed by the initial nucleation rate of chromia. This is due to the fact that the nucleation rate dictates the chromia grain size, and grain boundary diffusion of transition metals through Cr_2O_3 is significantly faster (3–5 orders of magnitude) than bulk diffusion [42]. Additionally, it has been reported that grain boundary diffusion of Mn is 1–2 orders of magnitude faster than the grain boundary diffusion of Cr or Fe in Cr_2O_3 [42, 43]. Magdefrau et al. investigated the annealing treatment of Crofer 22 APU for long-term (750 h) and also short time (5 h h). Based on their results, the microstructures of the scale in samples oxidized for just 5 h revealed that the nucleation of Cr_2O_3 and $MnCr_2O_4$ phases during the initial oxidation stages influenced the ultimate scale microstructures. Larger alloy grain sizes resulted in lower nucleation rates, larger spinel grains, and enhanced oxidation resistance. It is deduced from these findings that larger alloy grain sizes in heat-treated samples

diminish the initial supply of Mn to the alloy surface. This, in turn, leaves more Cr available to form a thicker initial Cr_2O_3 scale with coarser grains. Consequently, alloy heat treatment proves to be an effective method for slowing the oxidation of Crofer 22 APU [44]. However, in this study, the formed oxide layer should be able to close the pores of the substrates providing the surface for a thin defect-free Pd coating with a thickness of less than 10 µm (Fig. 8).
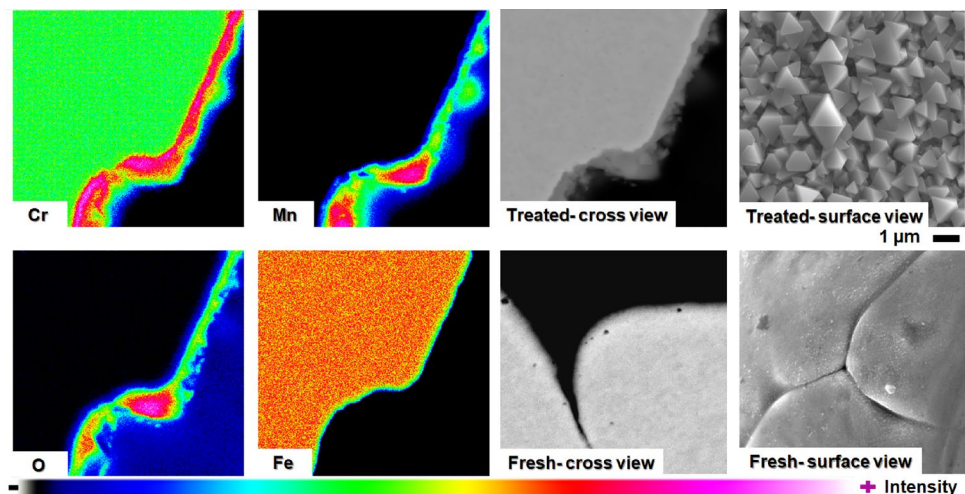
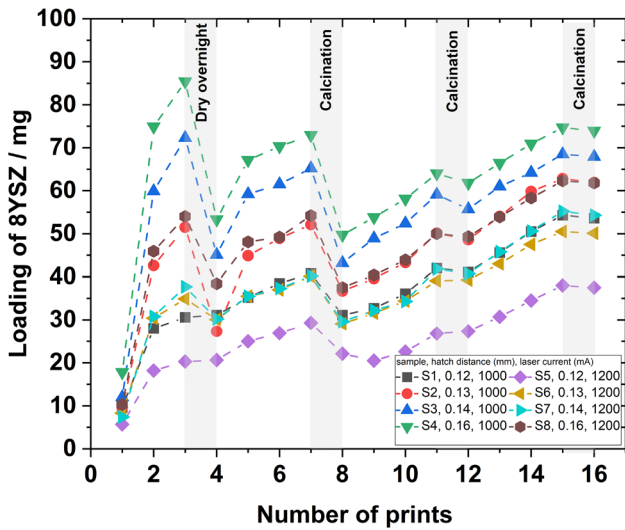## 4.2 Screen printing coating

To apply a protective layer to the permeable sections of the additively manufactured (AM) plates, the screen printing technique was employed. This method is well-suited for coating flat structures with varying layer thicknesses, depending on the number of print jobs. In this study, no pretreatment such as polishing of the AM samples was performed. A printing paste consisting of ytteria-stablized zirconia (8YSZ, TZ-8Y, Tosoh, Japan), Terpineol 98% (Alfa Aesar), dispersant (Hypermer KD1-SO-(AP)), and ethyl cellulose (viscosity 100 cp, Aldrich) was prepared. After mixing the ingredients on a heater stirrer, the formed paste was rolled for 30 min by a three-roll milling. All print jobs were carried out under consistent conditions for all samples simultaneously. After screen printing, the samples were held in an oven at 40 °C for 2 h. Before each new print job, the deposited weight of the previous step was recorded. Calcination at 550 °C for 2 h with heating rate of 2K min^{-1} was performed after several printing-drying jobs.

4.2.1 Results of coated porous parts with screen printing technique

Figure 9 shows the weight deposition changes versus surface properties of samples S1–S8. It is seen, with enlarging in hatch distance from samples S1 to S4 and also from samples

Fig. 8 Heat treatment under Air atmosphere for sample S5, at 800 °C for 2 h

Fig. 9 Deposition weight records versus number of screen printing jobs for printed samples S1–S8 (hatch distance 0.12 mm to 0.16 mm and laser current 1000 mA to 1200 mA)

S5 to S8, the weight of depositing increases. It might be justified with the effect of surface roughness and also the volume of paste in contact with plates that penetrate inside the pores [45]. Sample S4 with maximum hatch distance and minimum laser current compared to other samples shows the maximum loading of 8YSZ (73.9 mg), while sample S5 possesses the lowest deposition (37.5 mg). Given that all

screen printer parameters were kept constant, this variation indicates that the paste primarily covers the surface levels of the samples after 16 printing steps.

The quality of the coated samples also was analyzed by scanning electron microscopy (SEM) imaging. Figure 10 shows the surface view of the coated samples after screen printing process. At a magnification of 25 ×, defects such as uncovered spots were observed in samples S2–S4 and also S6–S8. These defects are attributed to the surface roughness of these samples.

Although additional printing jobs could improve coverage and coating on these samples, it is not advisable due to potential increases in mass transfer resistance and mechanical instability of the layer.

According to the results, sample S5 depicts a defect-free surface that provides a rather smooth surface for any later coating such as Pd-based active layer. Furthermore, Fig. 11 shows the cross-sectional view of the samples S1–S8, highlighting the depth of 8YSZ paste penetration into the porous support following the screen printing process. It is found that the penetration depth depends on the porous part structure and the sample S4 depicts a penetration depth of approximately 30% of the substrate thickness. It was not possible to measure the water contact angle (wettability test) for all samples as they were highly hydrophilic.

Figure 12 shows the surface roughness measurements of samples S1–S8 during various stages of the coating process. The results highlight the significant impact of the 8YSZ

Fig. 10 Surface view of coated samples with 8YSZ with screen-printing technique (hatch distance 0.12 mm to 0.16 mm and laser current 1000 mA to 1200 mA)
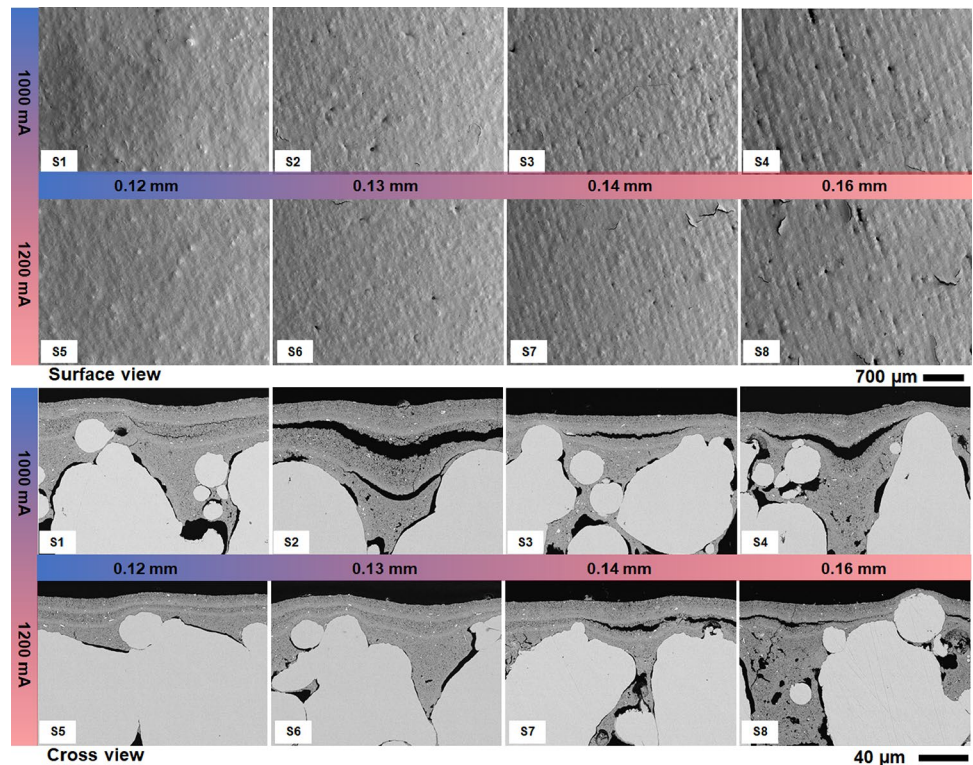
Fig. 11 Cross-sectional view of coated samples S1–S8; with magnification 50X. The effect of paste penetration when printing is shown (hatch distance 0.12 mm to 0.16 mm and laser current 1000 mA to 1200 mA)
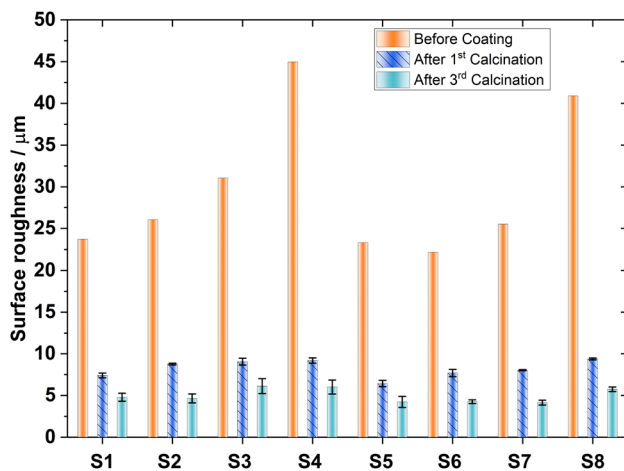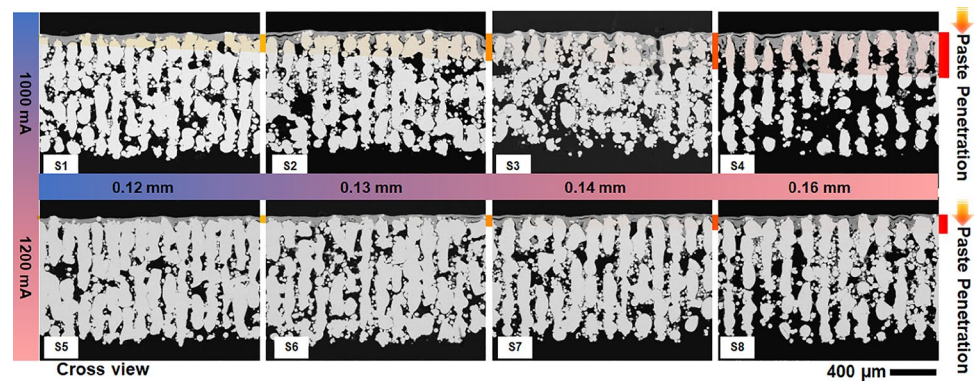
Fig. 12 Surface roughness variation of samples S1–S8 after coating of 8-YSZ with screen printing technique (hatch distance 0.12 mm to 0.16 mm and laser current 1000 mA to 1200 mA)

coating for reducing surface roughness. Notably, the difference in surface roughness between samples with high porosity, such as S4, and those with low porosity, such as S5, decreases markedly from 50% to 5%, emphasizing the impact of the 8YSZ coating. Nevertheless, since the 8YSZ exhibits the highest resistance to gas permeation (as Knudsen diffusion is expected), it is advisable to minimize the thickness of this layer. As illustrated in Fig. 11, the optimal case in this study is anticipated to be S5. It is important to note that for meaningful comparisons in gas tests, a defect-free coating is essential for all samples. In this study, only S5 is identified as having a defect-free surface based on the surface images. Testing for gas permeability of the samples is beyond the scope of this study and will be addressed in future research.

5 Conclusion

For the first time, this study developed process parameters for processing Crofer 22 APU using laser-based powder bed fusion. The capabilities of additively manufactured Crofer 22 APU were demonstrated on a metallic Pd membrane support as part of a membrane reformer for high-temperature applications. Through systematic parameter optimization, composite substrates comprising dense and porous structures were developed. Variations in hatch distance and laser power were used to evaluate the porosity and permeability of the substrates. A protective layer of 8YSZ was coated on the samples and analyzed. Additionally, objects built with different up-facing and down-facing angles of printing were examined. The integrated design simplifies assembly, reduces the number of welding operations, and allows for a thinner membrane reformer. The combination of screen printing coating and additively manufactured Crofer 22 APU reduces fabrication costs and time for membrane reactor plates, facilitating industrial scaling-up. The positive results of this study demonstrate the potential use of additively manufactured Crofer 22 APU not only as a membrane support but also for other reactor designs. This high-temperature, corrosion-resistant material expands opportunities in terms of operating conditions and design perspectives in chemical process engineering.

Declaration

References

1. Wunsch A, Kant P, Mohr M et al (2018) Recent developments in compact membrane reactors with hydrogen separation. Membranes 8(4):107

2. Boretti A, Banik BK (2021) Advances in hydrogen production from natural gas reforming. Adv Energ Sust Res 2(11):2100097

3. Van Hook JP (1980) Methane-steam reforming. Catalysis Rev Sci Eng 21(1):1–51

4. Obradović A, Likozar B, Levec J (2013) Catalytic surface development of novel nickel plate catalyst with combined thermally annealed platinum and alumina coatings for steam methane reforming. Int J Hydr Energy 38(3):1419–1429

5. Živković LA, Pohar A, Likozar B et al (2020) Reactor conceptual design by optimization for hydrogen production through intensified sorption-and membrane-enhanced water-gas shift reaction. Chem Eng Sci 211:115174

6. Obradović A, Likozar B, Levec J (2013) Steam methane reforming over ni-based pellet-type and pt/ni/al2o3 structured plate-type catalyst: intrinsic kinetics study. Indust Eng Chem Res 52(38):13597–13606

7. Amiri TY, Ghasemzageh K, Iulianelli A (2020) Membrane reactors for sustainable hydrogen production through steam reforming of hydrocarbons: A review. Chem Eng Process Intensif 157:108148

8. Li P, Wang Z, Qiao Z et al (2015) Recent developments in membranes for efficient hydrogen purification. J Membr Sci 495:130–168

9. Krzeminski P, Leverette L, Malamis S et al (2017) Membrane bioreactors-a review on recent developments in energy reduction, fouling control, novel configurations, lca and market prospects. J Membr Sci 527:207–227

10. Arratibel Plazaola A, Pacheco Tanaka DA, Van Sint Annaland M et al (2017) Recent advances in pd-based membranes for membrane reactors. Molecules 22(1):51

11. Mardilovich IP, Engwall E, Ma YH (2002) Dependence of hydrogen flux on the pore size and plating surface topology of asymmetric pd-porous stainless steel membranes. Desalination 144(1–3):85–89

12. Alique D, Martinez-Diaz D, Sanz R et al (2018) Review of supported pd-based membranes preparation by electroless plating for ultra-pure hydrogen production. Membranes 8(1):5

13. Dutta B, Dayal B (1963) Lattice constants and thermal expansion of palladium and tungsten up to 878 c by x-ray method. Phys Status Solidi 3(12):2253–2259

14. VDM Metals International GmbH (2021) VDM®Crofer 22 APU. Material Data Sheet No 414 https://www.vdm-metals.com/fileadmin/user_upload/Downloads/Data_Sheets/Data_Sheet_VDM_Crofer_22_APU.pdf

15. Ulan kyzy S, Voelkl R, Munz O et al (2020) Thermo-physical properties of hastelloy x and haynes 214 close to the melting range. Mater Sci Technol 36(10):1012–1019

16. Raju S, Sivasubramanian K, Divakar R et al (2004) Thermal expansion studies on inconel-600® by high temperature x-ray diffraction. J Nuclear Mater 325(1):18–25

17. Thyssenkrupp AG (2023) https://www.thyssenkrupp.com

18. Hadjixenophontos E, Mahmoudizadeh M, Rubin M et al (2022) Palladium membrane with high density of large-angle grain boundaries to promote hydrogen diffusivity. Membranes 12(6):617

19. Xie D, Dittmeyer R (2021) Correlations of laser scanning parameters and porous structure properties of permeable materials made by laser-beam powder-bed fusion. Addit Manuf 47:102261. https://doi.org/10.1016/j.addma.2021.102261

20. Kundra M, Grall T, Ng D et al (2021) Continuous flow hydrogenation of flavorings and fragrances using 3d-printed catalytic static mixers. Indust Eng Chem Res 60(5):1989–2002

21. Liu J, Gao Y, Fan Y et al (2020) Fabrication of porous metal by selective laser melting as catalyst support for hydrogen production microreactor. Int J Hydr Energy 45(1):10–22

22. Calignano F, Tommasi T, Manfredi D et al (2015) Additive manufacturing of a microbial fuel cell-a detailed study. Sci Rep 5(1):1–10

23. Rizzi C, Andrisano AO, Leali F, et al (2019) Design tools and methods in industrial engineering. In: Conference proceedings ADM, Springer, p 14

24. Stoffregen H, Fischer J, Siedelhofer C, et al. (2011) Selective laser melting of porous structures. In: Proceedings of the 22nd Annual International Solid Freeform Fabrication (SFF) Symposium. University of Texas, Austin, TX, pp 680–695

25. Gu D, Shen Y (2008) Processing conditions and microstructural features of porous 316L stainless steel components by DMLS. Appl Surf Sci 255(5):1880–1887. https://doi.org/10.1016/j.apsusc.2008.06.118

26. Yadroitsev I, Shishkovsky I, Bertrand P et al (2009) Manufacturing of fine-structured 3D porous filter elements by selective laser melting. Appl Surf Sci 255(10):5523–5527. https://doi.org/10.1016/j.apsusc.2008.07.154

27. Klahn C (2015) Laseradditiv gefertigte, luftdurchlässige Mesostrukturen: Herstellung und Eigenschaften für die Anwendung. Light Engineering für die Praxis, Springer, Berlin and Heidelberg. https://doi.org/10.1007/978-3-662-47761-8

28. Klahn C, Meboldt M (2015) Integration of gas-permeable structures in laser additive manufactured products. In: Srivatsan TS, Sudarshan TS (eds) Additive manufacturing: Innovations, advances, and applications. CRC Press LLC. p. 285–310

29. Xie D, Fränkle B, Klahn C et al (2022) Fabrication of sectionally permeable components with curved surface by laser-beam powder-bed fusion. Chem Ing Tech 94(7):983–992. https://doi.org/10.1002/cite.202200009

30. Li R, Liu J, Shi Y et al (2010) 316L stainless steel with gradient porosity fabricated by selective laser melting. J Mater Eng Perform 19(5):666–671. https://doi.org/10.1007/s11665-009-9535-2

31. Yasa E, Deckers J, Craeghs T, et al. (2009) Investigation on occurance of elevated edges in selective laser melting. In: Proceedings of the 20th Annual International Solid Freeform Fabrication (SFF) Symposium. University of Texas, Austin, TX, pp 180–192

32. Charles A, Elkaseer A, Paggi U et al (2021) Down-facing surfaces in laser powder bed fusion of Ti6Al4V: Effect of dross formation on dimensional accuracy and surface texture. Addit Manuf 46:102148. https://doi.org/10.1016/j.addma.2021.102148

33. Ferchow J, Biedermann M, Müller P et al (2021) Harnessing manufacturing elements to select local process parameters for metal additive manufacturing: A case study on a superconducting solenoid coil. Addit Manuf 46:102140. https://doi.org/10.1016/j.addma.2021.102140

34. Najmi H, El-Tabach E, Chetehouna K et al (2016) Effect of flow configuration on darcian and forchheimer permeabilities determination in a porous composite tube. Int J Hydr Energy 41(1):316–323

35. Zeng Z, Grigg R (2006) A criterion for non-darcy flow in porous media. Transp Porous Media 63(1):57–69

36. Martins J, Milton-Tayler D, Leung H (1990) The effects of non-darcy flow in propped hydraulic fractures. In: SPE Annual Technical Conference and Exhibition, OnePetro. SPE, pp SPE–20709–MS, https://doi.org/10.2118/20709-ms

37. Hassanizadeh M, Gray WG (1980) General conservation equations for multi-phase systems: 3. constitutive theory for porous media flow. Adv Water Res 3(1):25–40

38. Hassanizadeh SM, Gray WG (1987) High velocity flow in porous media. Transport Porous Med 2(6):521–531

39. Saeki I, Konno H, Furuichi R (1996) Initial oxidation of type 430 stainless steels with 0.09–0.9 mn in o2-n2 atmosphere at 1273 k. Corros Sci 38(9):1595–1612

40. Saeki I, Konno H, Furuichi R et al (1998) The effect of the oxidation atmosphere on the initial oxidation of type 430 stainless steel at 1273 k. Corros Sci 40(2–3):191–200

41. Rufner J, Gannon P, White P et al (2008) Oxidation behavior of stainless steel 430 and 441 at 800 c in single (air/air) and dual atmosphere (air/hydrogen) exposures. Int J Hydr Energy 33(4):1392–1398

42. Lobnig R, Schmidt H, Hennesen K et al (1992) Diffusion of cations in chromia layers grown on iron-base alloys. Oxid Met 37:81–93

43. Sabioni A, Huntz A, Borges L et al (2007) First study of manganese diffusion in cr2o3 polycrystals and thin films by sims. Philos Mag 87(12):1921–1937

44. Magdefrau NJ, Chen L, Sun EY et al (2013) Effects of alloy heat treatment on oxidation kinetics and scale morphology for Crofer 22 APU. J Power Sources 241:756–767

45. Krainer S, Hirn U (2021) Contact angle measurement on porous substrates: Effect of liquid absorption and drop size. Colloids Surf A: Phys Eng Asp 619:126503

Publisher's Note Springer Nature remains neutral with regard to jurisdictional claims in published maps and institutional affiliations.